DOI: 10.13009/EUCASS2022-4435
9TH EUROPEAN CONFERENCE FOR AERONAUTICS AND SPACE SCIENCES (EUCASS)

Hypersonic Retrograde Propulsion Experiments – A Basis for Validation of CFD within RETPRO

D. Kirchheck, A. Marwege, J. Klevanski, A. Gülhan
German Aerospace Center (DLR)
Supersonic and Hypersonic Technologies Department
Linder Höhe, 51147 Cologne, Germany
daniel.kirchheck@dlr.de

Abstract

The paper focuses on wind tunnel tests of the hypersonic re-entry part of the RETPRO descent trajectory. The re-usable rocket launcher configuration is investigated including active retro-propulsion at Mach 5.3 and 7.0 in the Hypersonic Wind Tunnel (H2K) of DLR, Cologne. Results from high-speed Schlieren imaging, force and unsteady wall pressure measurements are output for CFD accuracy assessment and validation. Variations of the number of active engines, thrust coefficient, jet temperature and angle of attack are performed to gather detailed information on sensitivities of characteristic mean and dynamic flow features. It is shown that the dynamic behavior of the retro-propulsion flow field is significantly altered by the engine configuration. A stable quasi-steady mode with overlaying shock oscillation is found for the one engine case, while three engine operation leads to a turbulent flow field with random flipping between a short and a long jet penetration mode. The oscillation frequency and temporal characteristics of the retro-propulsion flow field are found to be sensitive to the thrust coefficient and jet reservoir temperature.

1. Introduction

The RETPRO project (*Validation of Wind Tunnel Test and CFD Techniques for Retro-propulsion*), as part of ESA's *Future Launchers Preparatory Programme* (FLPP) [1], aims at preparing the tools, necessary for a reliable design and simulation of future rocket launchers in view of the European goal to access the field of re-usability using retrograde propulsion for vertical powered descent and landing. The tools, that are necessary for an aerodynamic design include *Wind Tunnel Tests* (WTT) and *Computational Fluid Dynamics* (CFD) in order to generate a comprehensive aerodynamic database, essential for flight dynamics simulations, enabling mission and performance analyzes of potential future launcher designs. The validation of WTT and CFD techniques is performed by both complementary and comparative experimental and numerical studies on common reference test cases for the underlying RETPRO launcher concept with a close link to the operational SpaceX Falcon 9 vehicle (Fig. 1). [2] The study includes down-scaled wind tunnel tests in the hypersonic, supersonic and subsonic regimes, using pressurized air and hot gas from a model-integrated combustion chamber to simulate the retro-propulsive jets. The results will provide a valuable foundation for validation of CFD codes in the respective flow regimes, ultimately being facilitated to extrapolate the established models to flight relevant scales in order to populate the databases for final flight analyzes.

The present paper focuses on the wind tunnel experiments at Mach 5.3 and 7.0, conducted in the *Hypersonic Wind Tunnel* (H2K) at the *German Aerospace Center* (DLR), Cologne. The test conditions are set to duplicate a high-altitude, so called, re-entry burn maneuver, similar to the flight profile of SpaceX's Falcon 9, which serves as basis for the underlying reference configuration, presented in [2] (see Fig. 2). The wind tunnel model is equipped with a 4-/6-component strain gauge balance to measure aerodynamic forces. The flow topology is being assessed, using Schlieren optical visualization enabling modal analysis of the highly unsteady flow field. The pressure field is characterized at selected locations at the engine bay and along the cylindrical body using high-frequency pressure transducers as output for CFD accuracy assessment and validation as well as validation of the Schlieren dynamics evaluation. Information on the CFD rebuilding of the reported test cases can be found in [5]. The different measurement techniques are used to work out sensitivities from several parameter variations, including Mach number variation, thrust coefficient, jet temperature and angle of attack. The paper introduces the test facility, setup, design, and capabilities of the wind tunnel model including implemented instrumentation. It provides an overview on the mean flow topology and dynamic flow features depending mainly on the engine layout and the temperature of the retro-propulsive jet.

The results can be compared to other works, in which a similar configuration, RETALT [6], is investigated w. r. t. aerodynamics on a powered descent trajectory at similar trajectory points. [7, 8]

DOI: 10.13009/EUCASS2022-4435

Figure 1: Image of a Falcon 9 first stage booster performing a three engine hypersonic retro-propulsion maneuver during atmospheric re-entry [3] (refer to [4] for video comparison)

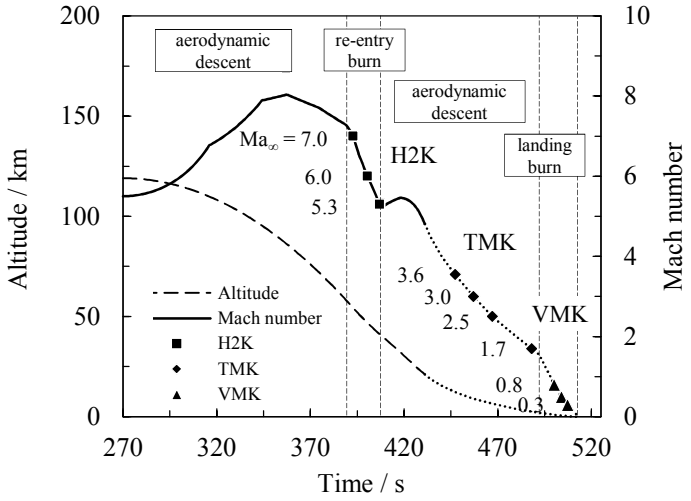

Figure 2: Experimental reference trajectory based on the SpaceX Falcon 9 GTO reference mission (SES-11) webcast telemetry data; dotted lines express trajectory extrapolation caused by an interrupted telemetry stream [2]

2. Experimental Setup and Methods

2.1 Wind Tunnel Facility and Test Setup

The facility, used for the aerodynamic tests in the hypersonic regime is the *Hypersonic Wind Tunnel Cologne* (H2K) of the *German Aerospace Center* (DLR) (Fig. 3). It is a blow-down facility with a free jet test section using a dried air pressure reservoir on the primary side and a vacuum reservoir on the secondary side. Its operating range is between Mach 5.3 and 11.2 using exchangeable nozzles with 600 mm nozzle exit diameter. Details on the operating range, stating the mass flow and Reynolds number regimes for the different nozzles are provided in Fig. 4. The primary air is heated by electric heaters up to 1 000 K in order to mitigate condensation after expansion to static conditions, as well as for adjusting the freestream Reynolds number. Typical test durations are about 30–60 s run time. The secondary supply of the model in order to simulate the engine plume uses the same pressurized air reservoir. Dried air is either fed at room temperature conditions or heated by an additional electric heater up to approximately 750 K at about 55 bar maximum supply pressure. Constant test conditions are reached before redirecting the primary and secondary streams to the test section and through the model outlet using 3/2-way valves. Consequently, this test setup provides high repeatability of test conditions. The wind tunnel model (Fig. 5 and 6) is held in the test section on the freestream centerline at approximately 200 mm downstream of the wind tunnel nozzle exit plane. Here, it is placed in the optics path, such that one high-resolution and one high-speed camera are able to capture the upstream flow field and part of the models rear body.

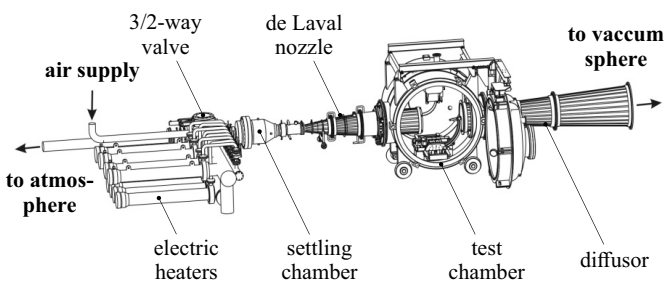

Figure 3: Hypersonic Wind Tunnel Cologne (H2K)

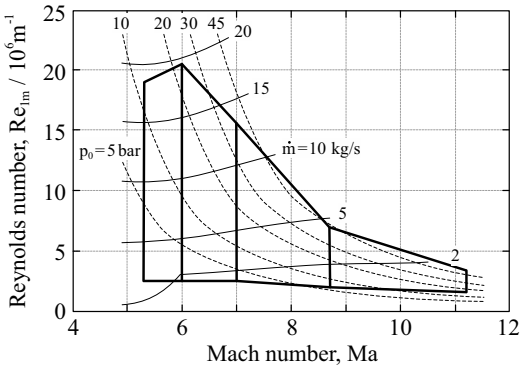

Figure 4: H2K operating range

DOI: 10.13009/EUCASS2022-4435

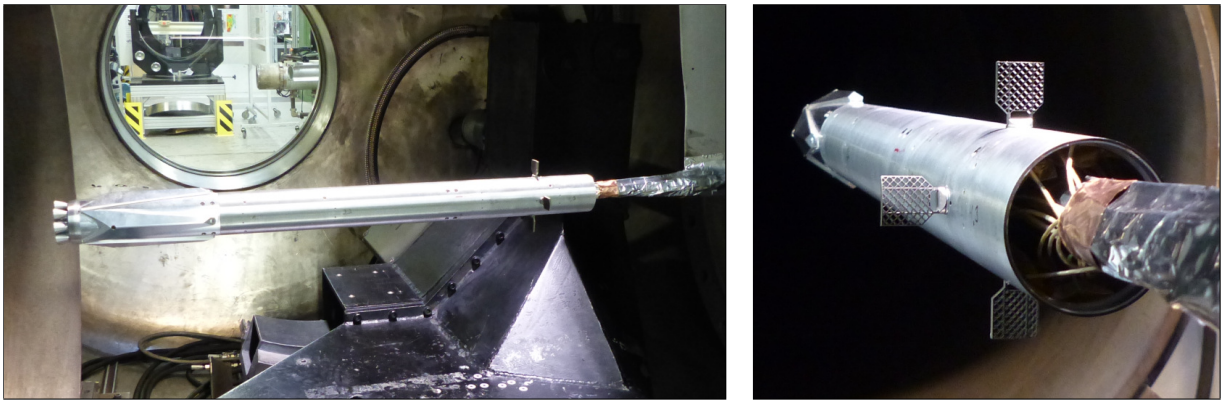

Figure 5: RETPRO full length wind tunnel model integrated in the H2K facility

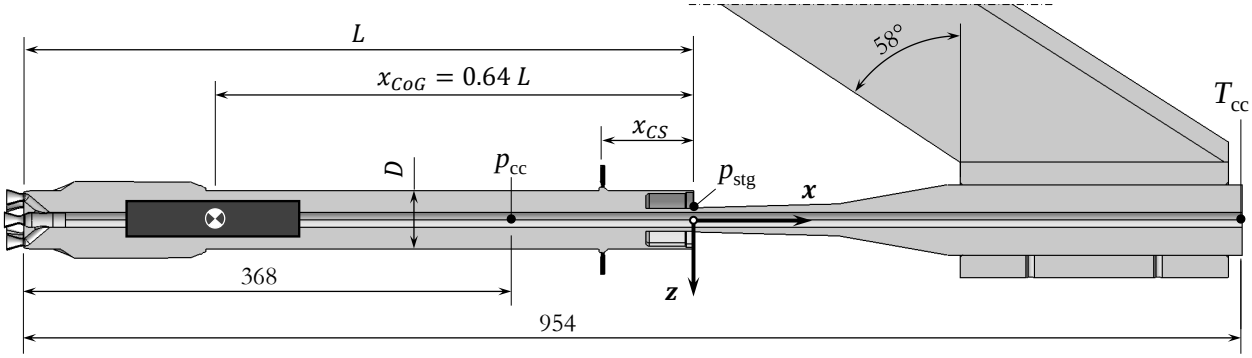

Figure 6: Sketch of the RETPRO wind tunnel model for hypersonic retro-propulsion with 4/6-components force balance and unsteady wall pressure measurements, integrated in the H2K facility using a 58° strut support

2.2 Wind Tunnel Model

Two types of wind tunnel models with a scaling of 1/80, resulting in a main diameter $D = 45.75$ mm and length $L = 578.5$ mm were used for the tests. Both were used for usual and high-speed Schlieren (HSS), force, and pressure measurements. The model of the RETPRO full length configuration (Fig. 5) was primarily used for tests on different angle of attack and control surface configurations without active plume. Tests with active plume were performed on a shortened version with a length $L_{\text{short}} = 0.55L$ in order to fit model and plume into the undisturbed core flow region. While 6-component force balances were used for the full length model, the shortened active plume model was equipped with a tubular 4-component balance, providing air supply to the nozzle section.

The model features exchangeable nozzle sections and control surfaces, providing means to vary the number of active engines with expansion ratio $\varepsilon = 5$ between zero, one and three (center engine or three engines in the vertical plane active) and control surfaces between none, grid fins, or planar fins with deflection angles of ±20° in steps of 5° for different validation opportunities of CFD. The force balance was placed in the assumed center of gravity (CoG) of the underlying RETPRO reference configuration at $x_{\text{CoG}} = 0.64L$. The reference configuration is presented in [2]. The results from force measurements provided vital information for CFD validation that are not provided in the paper. More information on the CFD validation can be found in [5].

At the model, next to force measurements, the total outflow conditions p_{cc}, T_{cc}, the static base pressure p_{stg} and unsteady wall pressures were measured at different locations, pictured in Fig. 7. Unsteady pressures were measured using Kulite® pressure transducers. At the engine bay (Fig. 7, left), XCQ-080-0.7BARA sensors were used with a transmission path of approximately D0.5×50 mm. Along the main cylinder (Fig. 7, right), LQ-062-0.7BARA were applied just beyond the surface with a transmission path D0.5×0.5 mm. Measurement locations at the engine bay (0–7) were connected to the sensors via additively manufactured tubing through the base part, which needs to be accounted for in the evaluation of their spectral response since perfectly equal paths cannot be assured.

DOI: 10.13009/EUCASS2022-4435

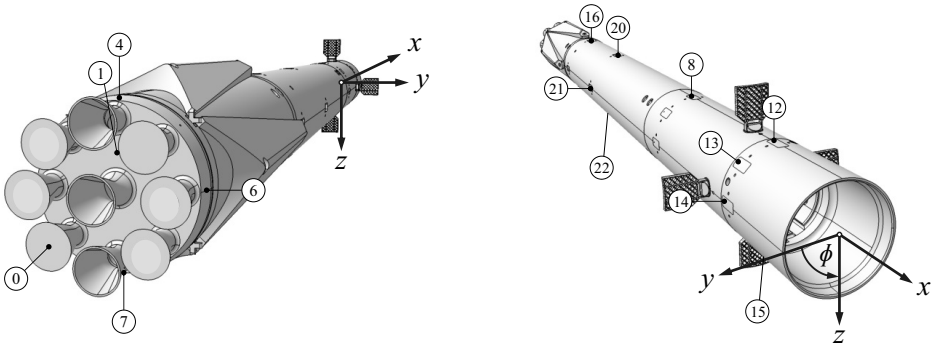

Figure 7: Sensor locations for unsteady pressure measurements on the RETPRO full length model at the engine bay (left) and along the main cylinder (right); for the short model version, locations 16–22 were not applied

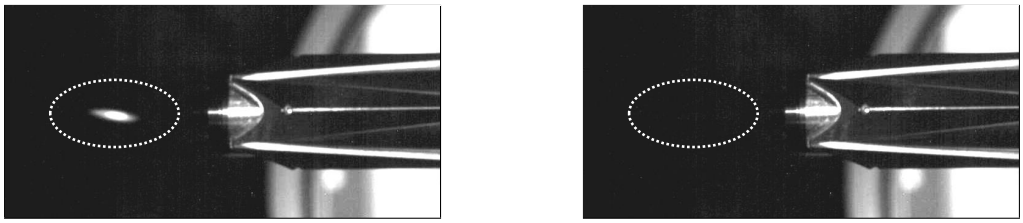

Figure 8: Condensation in the ambient temperature jet of a retro-propulsion flow field, visualized using laser light sheet illumination (left), mitigated at higher reservoir conditions (e. g. V111, V112, right)

2.3 Test Cases and Test Conditions

The tests presented in this paper were performed at Mach 5.3 using 12.5 bar at 400 K reservoir temperature. Expansion in the wind tunnel nozzle leads to the measured static conditions given in Table 1. Cold plume tests and hot plume tests were performed in single plume and multi-plume configurations. For the model outflow, the reservoir pressure was set to nominal values of 34.99 bar for single plume cases and 27.64 bar for multi-plume cases, respectively, in order to aim for a constant total thrust coefficient $C_T \approx 4.9$ (including all active engines) at a nominal nozzle exit Mach number $M_e = 3.18$ as reference. Regarding hot plume tests, reservoir temperatures for the model outflow between 675 K and 745 K were reached. Additional tests were performed applying a p_{cc}-transient from zero to maximum in order to find the highest possible model pressure without provoking influences on the wind tunnel core flow region and in order to analyze sensitivities of flow features and wall pressures with respect to C_T.

Tests with heated supply air were performed in order to analyze the impact of condensation and temperature ratio on the flow topology and dynamic flow features. In the retro-propulsion flow field, the jet is subject to post-expansion, leading to high external Mach numbers on the order of 8. The respective temperature drop leads to significant condensation in the retro-propulsion flow field, visualized in Fig. 8, left, for the current test setup via local laser light sheet illumination. Condensation is to the greatest extend mitigated for the hot plume test cases V111, V112 (Fig. 8, right). Although, local static pressures might still rise above the specific oxygen and nitrogen vapor pressures, resting times of molecules in this flow region are too short for condensation nuclei to form (see [9] for more detailed information).

Table 1: Measured static wind tunnel and jet reservoir conditions for selected test cases

Case no.	Plume type	p_∞ mbar	T_∞ K	p_{cc} bar	T_{cc} K	C_T –
V038*	Single plume, cold, p_{cc} sweep	7.07	60.28	0 . . . 46.3	294.87	0 . . . 6.4
V061	Single plume, cold	7.08	60.10	34.55	292.92	4.834
V111	Single plume, hot	7.06	60.33	33.19	676.87	4.656
V039*	Multi-plume, cold, p_{cc} sweep	16.32	59.81	0 . . . 34.0	295.39	0 . . . 6.0
V044	Multi-plume, cold	16.44	60.55	27.66	293.38	4.961
V112	Multi-plume, hot	16.28	60.25	26.64	743.11	4.824

*V038 and V039 were performed as p_{cc} sweeps, running from zero to maximum in a single test run

DOI: 10.13009/EUCASS2022-4435

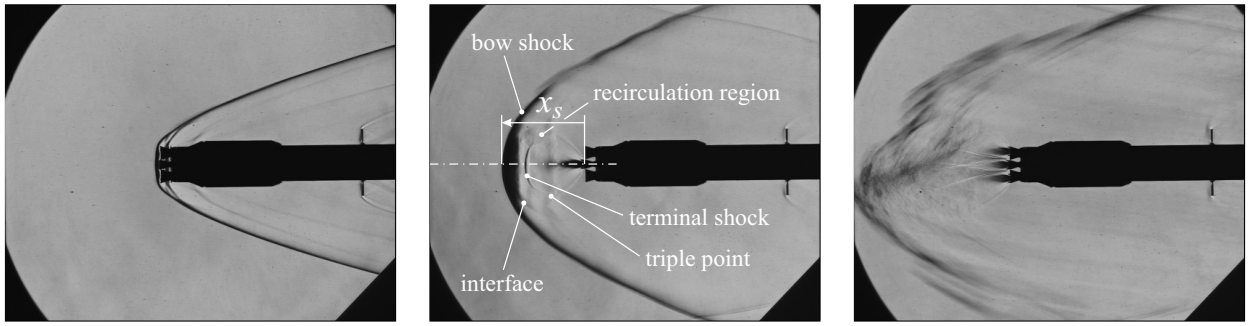

(a) no plume (b) cold single plume (V061) (c) cold multi-plume (V044)

Figure 9: High-resolution Schlieren images for an active engines variation at Mach 5.3 using ambient temperature air at thrust coefficicent $C_T \approx 4.9$; x_s is the shock stand-off distance (refer to [10] for video footage at Mach 7)

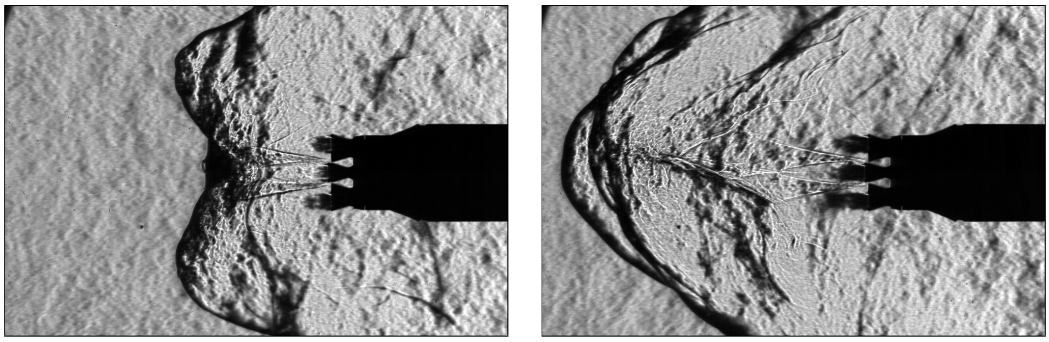

Figure 10: High-speed Schlieren snapshots, showing the different jet penetration modes, *short penetration mode* (left) and *long penetration mode* (right), for a cold multi-plume configuration (V044) at thrust coefficient $C_T \approx 4.9$

3. Results

3.1 Flow Topology

The general flow topology is examined mainly for two cold plume cases as well as an additional no plume case in Fig. 9, representing high resolution Schlieren images with an exposure time of approximately 8 ms, taken from video recordings at 120 fps (refer to [10] for a video showing single and multi-plume operation at Mach 7). For the no plume case, the shock structure shows to be a combination of shocks standing in front on the center nozzle, the peripheral nozzles and the shoulder of the engine bay (Fig. 9a). They merge downstream of the shoulder of the engine bay with the main contribution coming from the shocks in front of the peripheral nozzles. Note that although the nozzles cover a big part of the engine bay, a significant part of the flow impinging on the engine bay is still supersonic. On the centerline, the bow shock is slightly extended upstream, due to the center nozzle being slightly offset in the axial direction. Compression and re-compression waves, emerging from model features are visible in the vicinity of the landing legs and control surfaces, showing that the whole body is embedded in highly supersonic flow.

In case of the cold single plume (Fig. 9b), the flow field follows the principal features, described in theory in [11] and applied more recently in [12, 13, 14]. The typical retro-propulsion flow field, including the detached *bow shock* decelerating the incoming flow, *terminal shock* decelerating the jet flow, *interface* defining the free stagnation point on the centerline and the streamline between the incoming flow and the jet flow, as well as the *recirculation region* around the triple point is visible. The shock structure is quasi stationary, the stand-off distance of the detached bow shock is constant in time. However, a smearing of the outer bow shock, caused by the relatively long exposure, indicates what is clearly detectable from the recordings as a periodic oscillation of the detached bow shock. Further, downstream of the retro-propulsion flow field, no compression or re-compression waves are visible at the body until upstream of the control surfaces, indicating that the rear part of the vehicle is embedded in subsonic flow.

In case of the cold multi-plume (Fig. 9c), the interaction between the jets obviously causes a significant instability of the retro-propulsion flow field. The detached bow shock is rather represented as a system of many smaller shock structures, chaotically and independently propagating in the upstream direction. No clear interface nor terminal shock can be spotted in the instantaneous Schlieren images. The actual shock stand-off distance fluctuates to a wide extent,

DOI: 10.13009/EUCASS2022-4435

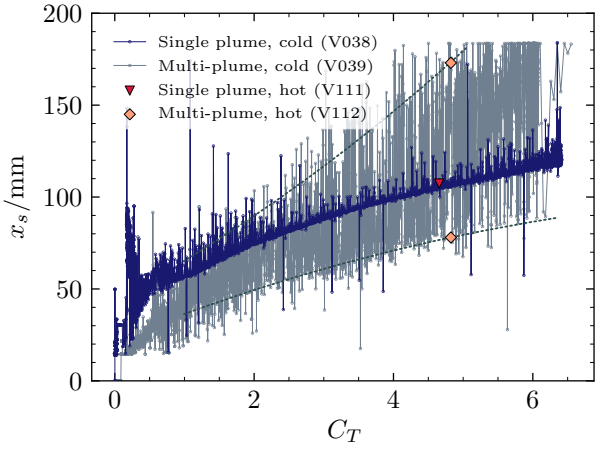

Figure 11: Shock stand-off distance, acquired from high-resolution Schlieren images versus thrust coefficient, for cold/hot single and multi-plume configurations

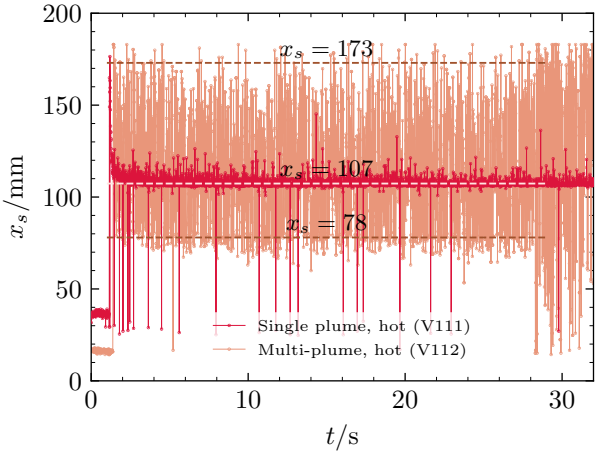

Figure 12: Shock stand-off distance, acquired from high-resolution Schlieren images versus time, for hot single and multi-plume configurations

however, seemingly randomly snapping in in the vicinity of two characteristic lengths, pictured in Fig. 10 as snapshots from the high-speed Schlieren recordings, taken with an exposure time of 2.5 μs at 20 000 fps. Refering to [15], they are called *short penetration mode*, also *blunt mode* (Fig. 10, left), and *long penetration mode* (Fig. 10, right), similar to the single plume situation. As for the single plume case, no further compression or re-compression waves are visible along the body, except for those at the control surfaces. Comparing the strength of the shocks in front of the control surfaces, it appears that the shadowing effect of the detached bow shock is strongest for the single engine case and weakest for the no plume case. This statement can be confirmed, when evaluating the forces on the body, which are minimal in case of the single plume and maximal in case of the no plume situation, leading to the known vanishing of the pressure drag coefficient during supersonic retro-propulsion [15] (forces not plotted in this paper).

3.2 Shock Stand-off Distance

A more detailed investigation of the bow shock stand-off distance x_s is provided in Fig. 11 for cold single and multi-plume cases versus the thrust coefficient and in Fig. 12 for hot single and multi-plume cases for a specific $C_T \approx 4.9$. The shock stand-off distance is acquired from the high-resolution Schlieren recordings (compare Fig. 9b) by applying a simple threshold to the grayscale values on the centerline between the left image boundary and the model. Since this method does not imply edge detection algorithms, the results – in particular those of the single plume cases – are more noisy than the visible fluctuation level suggests in the recordings. However, it is clearly visible that the characteristic behavior of the fluctuations in the single and multi-plume cases is as described for Fig. 9. The course of x_s is approximately proportional to $\sqrt{C_T}$, as already stated in [11, 15] and recently shown for a similar configuration in [7]. The plot shows the continuously prevailing blunt mode for the single engine case as well as a random flipping between the blunt or short penetration mode and the long penetration mode for the multi-plume case. Interestingly, the multi-plume short penetration mode follows the same square root law offset from the single plume case, whereas the characteristic course of the long penetration mode differs from that. Finally, the multi-plume short penetration mode predominantly appears at a different level more closely to the single plume case from $C_T \approx 5$ upwards, a trend that can also be found in [7]. Clarification is necessary, whether this trend continues for higher thrust coefficients, which would be relevant for extrapolation to fligt.

The hot single and multi-plume cases, plotted in Fig. 12 show the same characteristic modes over time at constant thrust coefficients. The estimated stand-off distances for the different modes are marked in the Figure using dashed lines. These data points are also given in Fig. 11, where they are compared with the cold plume cases at the specific C_T values. The comparison shows, that neither temperature nor condensation significantly influences the shock stand-off distance for the given cases.

3.3 Dynamic Flow Features

The dynamics of specific flow features that are already mentioned in the frame of Fig. 9 are investigated in more detail by a spectral analysis of the high-speed Schlieren recordings in Fig. 13, 14. Single snapshots of the processing

DOI: 10.13009/EUCASS2022-4435

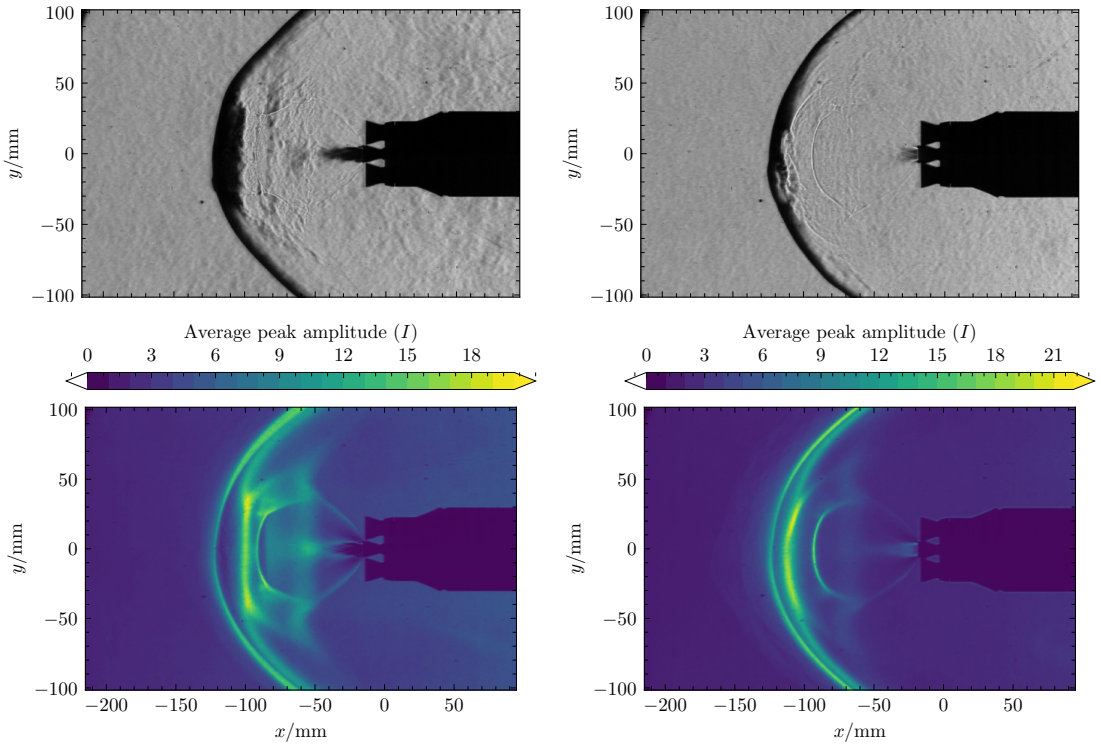

(a) cold single plume (V061)

(b) hot single plume (V111)

Figure 13: Snapshots of high-speed Schlieren recordings and average peak amplitude distribution of the Schlieren intensity fluctuations in the retro-propulsion flow field for the single plume cases (V061, V111)

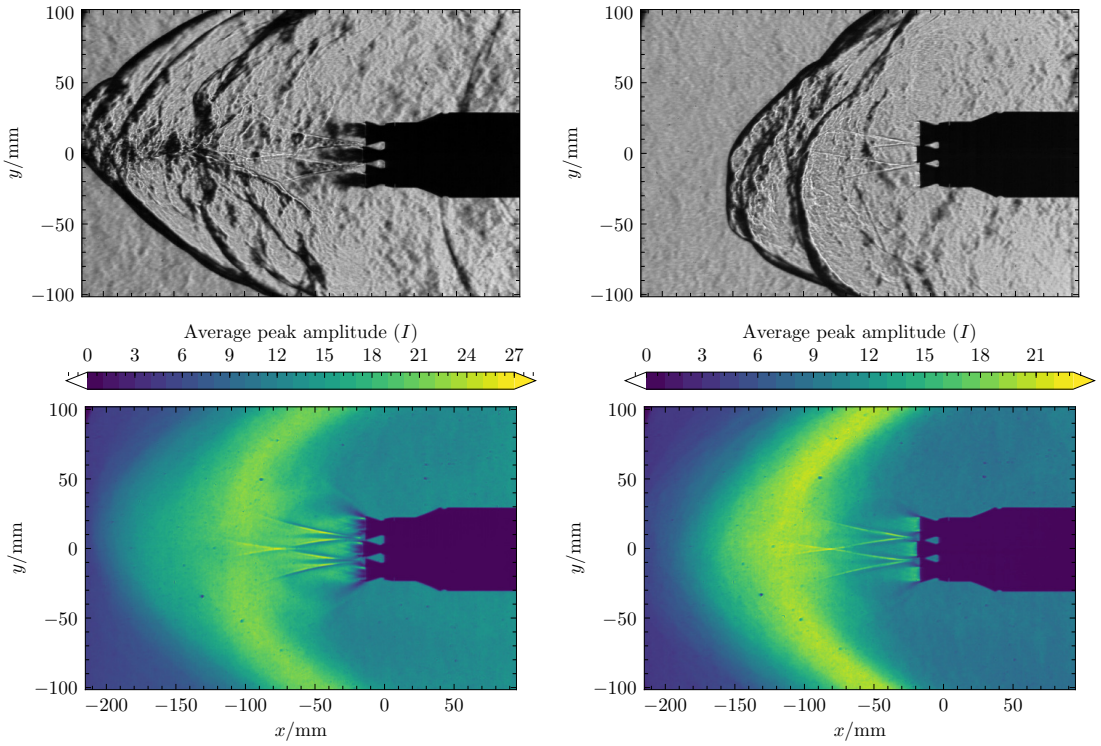

(a) cold multi-plume (V044)

(b) hot multi-plume (V112)

Figure 14: Snapshots of high-speed Schlieren recordings and average peak amplitude distribution of the Schlieren intensity fluctuations in the retro-propulsion flow field for the multi-plume cases (V044, V112)

DOI: 10.13009/EUCASS2022-4435

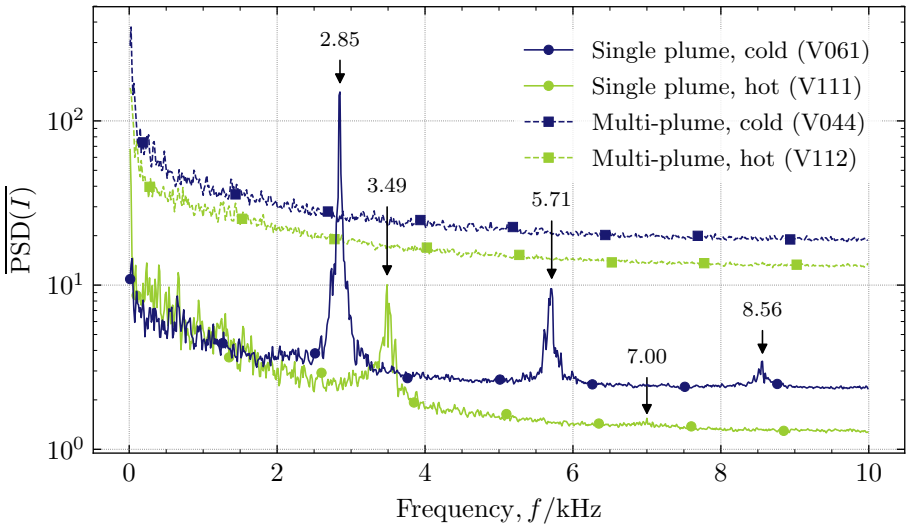

Figure 15: Spacially averaged power spectral density from high-speed Schlieren recordings, revealing major flow field fluctuation frequencies for the cold/hot single and multi-plume configurations

windows are provided at the top of the figures. At the bottom, the results of a pixel by pixel FFT analysis of the Schlieren intensity I is provided as the average peak amplitude of all frequencies for each the cold and hot plume tests.

For the single plume case (Fig. 13), it is visible in the snapshots that the density gradients are less pronounced at higher jet reservoir conditions. In the cold plume case, strong gradients lead to blackening in the vicinity of the contact surface, which needs to be accounted for in the discussion of the amplitude distribution. However it is evident that average fluctuation amplitudes are high around the bow shock, the terminal shock, and the contact surface for both, the cold and hot plume cases, while for the cold plume the fluctuation in spatial direction appears larger, leading to the assumption that the hot plume flow field is more stable. For the cold plume, fluctuation intensities in the vicinity of the triple point are also increased compared to the hot plume case. This roots from a periodic vortex roll-up and shedding mechanism that is more subtle in the hot plume case. Another periodic vortex shedding mechanism, reported in [7], taking place on the centerline near the interface cannot be detected. This, however, might be caused by the blackening in this specific flow region.

In the multi-plume situation (Fig. 14), generally, the distribution of the fluctuation amplitudes is much more disperse, confirming the impression of a highly unsteady flow field. Qualitatively, it appears in the recordings that the flipping between short and long penetration modes happens at a lower frequency under hot plume conditions. Further, the short penetration mode seems to be favored on a cumulative time basis in this case. Quantitatively, this impression is confirmed by the intensity distribution of the fluctuation amplitudes comparing the cold and hot multi-plume cases – for the hot case, the higher amplitudes are more confined to the short penetration regime.

In order to identify the most prevailing frequencies in the flow field, a spatial average of the power spectral density (PSD) of the Schlieren intensity I is provided in Fig. 15 for the cold and hot single and multi-plume cases. Here, it is to be noted that the amplitudes cannot directly be compared between different test cases regarding quantitative analysis of the respective fluctuations in the flow – the amplitudes depend largely on the optical setup and the conditions of the flow. However, the spectral distribution within specific test cases and of course the localization of specific frequency peaks is conclusive. In the cold plume case, a dominant frequency peak occurs at 2.85 kHz with harmonics at 5.71 kHz and 8.56 kHz, which by analyzing the spatial distribution of the isolated frequencies can clearly be traced back to the oscillating shock structure. Under hot plume conditions, the same phenomenon is shifted to 3.49 kHz, repeating at 7.00 kHz, but with a stronger dampening than in the cold plume case. This frequency shift seems reasonable, considering the higher flow velocities and higher speed of sound in the hot plume case. Comparing the level of noise between cold and hot plume, it shows that although low frequency noise is at a comparable level, the high frequency content is significantly higher in the cold plume case. This is caused by a bend of the cold plume spectrum at about 1.7 kHz which seems to be a specific feature of the cold plume flow dynamics.

For the multi-plume cases, no distinct frequencies can be detected, which under the assumption of a chaotic flow field is to be expected. The spectra of the cold and hot plume tests merely differ, expect for an offset in the amplitude level, which needs to be connected to the lower density level of the flow in the hot plume situation. Therefore, it is to be concluded that the temperature, hence condensation has no impact on the dynamics of the flow for the given cases.

DOI: 10.13009/EUCASS2022-4435

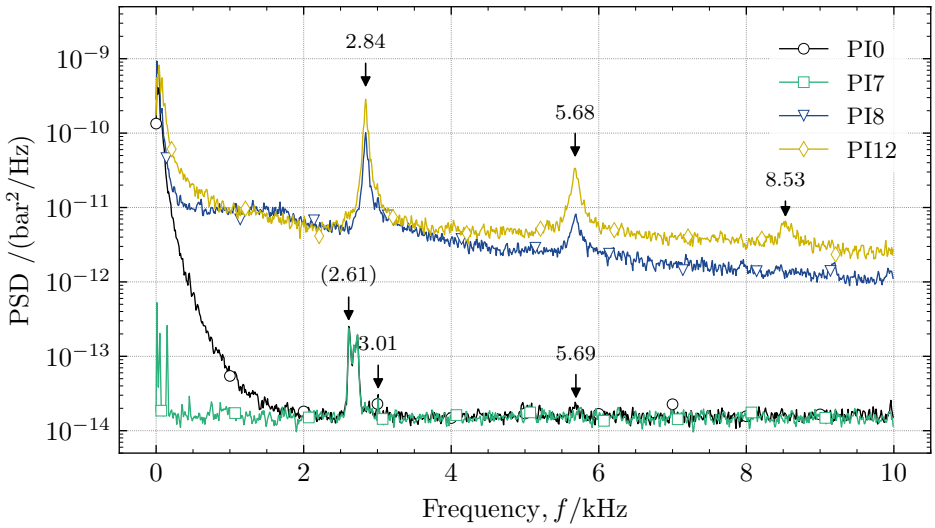

Figure 16: Power spectral density of wall pressure fluctuations for the *cold single plume* configuration (V061) at different sensor locations on the engine bay (PI0, PI7) and on the upper side along the main cylinder (PI8, PI12)

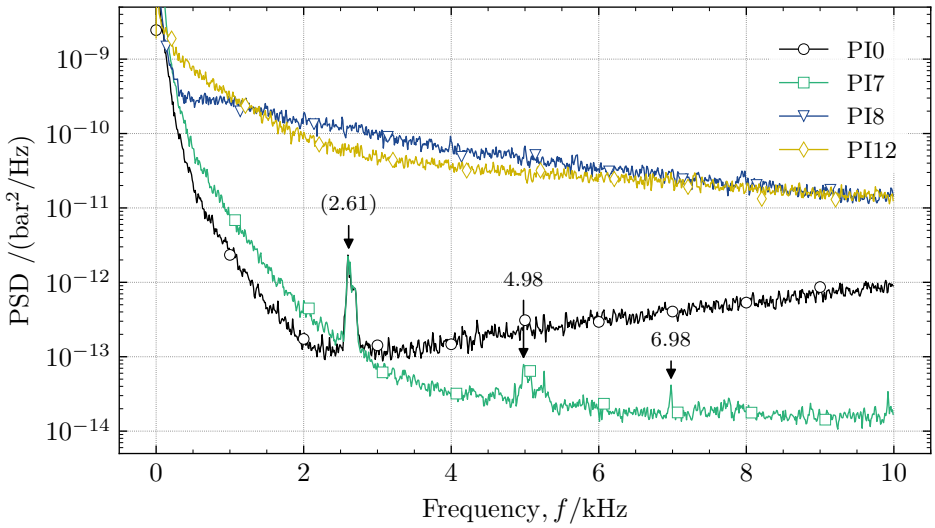

Figure 17: Power spectral density of wall pressure fluctuations for the *cold multi-plume* configuration (V044) at different sensor locations on the engine bay (PI0, PI7) and on the upper side along the main cylinder (PI8, PI12)

3.4 Wall Pressure Spectra

Next to additional insight, a validation of the HSS analysis can be obtained from an investigation of the unsteady wall pressures, provided in Fig. 16, 17 as power spectral density at different measurement locations for the cold single and multi-engine cases. The PSD is performed on a 4 s measurement interval with a sampling rate of 50 kHz. It uses a Hann window with an overlap of 0.5 in order to reach a frequency resolution of 10 Hz (compared to 12.5 Hz in the Schlieren analysis). For the single plume case (Fig. 16), the dominant peaks revealed by the Schlieren investigation are reproduced in the pressure spectra with very little deviation. However, they are only found dominant in the readings of sensors PI8 and PI12 (next to others that are not plotted here), which are located at the main cylinder with a minimal transmission length, as described in Section 2.2. As from the Schlieren analysis, the same sensors do not show any dominant peaks in the multi-plume case, visible in Fig. 17. But, the general noise level at these locations is indeed approximately one order of magnitude higher in the multi-engine case, which is comparable to the Schlieren evaluation when looking at either cold or hot cases only. This means that the Schlieren evaluation could possibly be used as a quantitative measure on a relative basis, when comparing similar flow conditions w. r. t. flow density.

Due to the long transmission length of sensor positions PI0 and PI7, located at the engine bay, a frequency analysis is to be seen critical. The noise level decreases drastically in the low frequency range, showing the dampening

DOI: 10.13009/EUCASS2022-4435

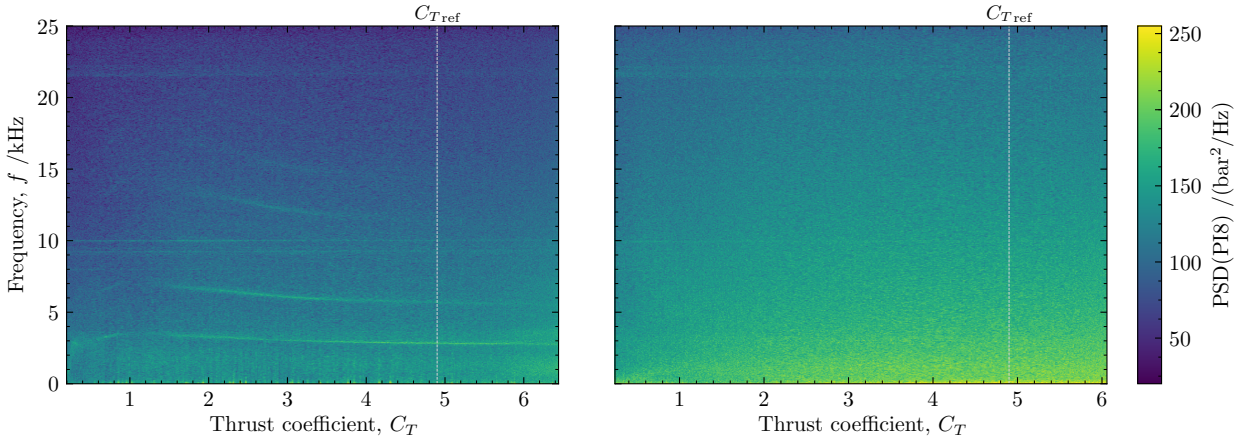

Figure 18: Variation of the power spectral density of wall pressure fluctuations over a thrust coefficient transient for the *cold single plume* configuration (V038, left) and the *cold multi-plume* configuration (V039, right) at location PI8

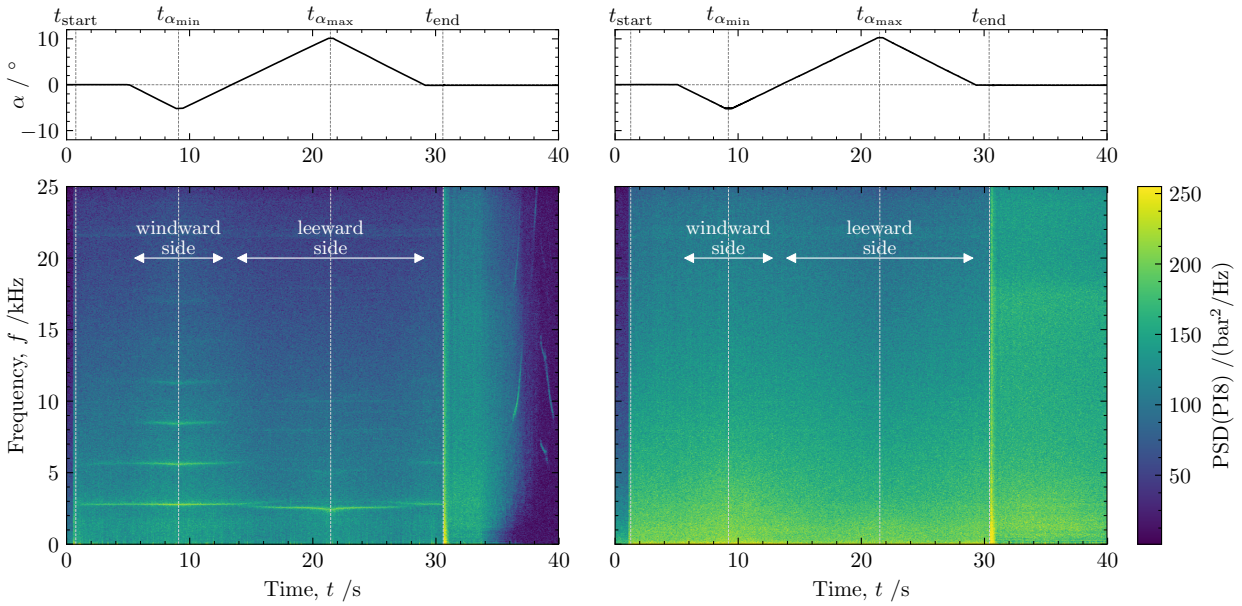

Figure 19: Variation of the power spectral density of wall pressure fluctuations over an angle of attack transient for the *cold single plume* configuration (V061, left) and the *cold multi-plume* configuration (V044, right) at location PI8

of the transmission path. However, dominant peaks that are not overlaid by other phenomena can actually be identified, as for example at 5.69 kHz in Fig. 16. This means that certain information can be drawn from the spectra after careful interpretation. In this regard, the peaks at 4.98 kHz and 6.98 kHz for the multi-plume case (Fig. 17) could be seen. These are neither visible in the spectra of the cylinder wall pressures, nor in the Schlieren evaluation, but might characterize specific local flow features in close vicinity of the engine bay, which cannot be resolved by the Schlieren system and which do not impact the readings of sensors farther downstream after being dampened by the highly unsteady flow. The peak at 2.61 kHz, found in the readings of PI0 and PI7 in both, the single and multi-plume cases ought to be excluded from interpretations w. r. t. flow physics, since it is assumed to root from acoustic properties of the specific sensors implementation.

3.5 Sensitivity Studies

The wall pressure spectra are examined over thrust coefficient and angle of attack transients for sensitivity analysis. The resulting spectrograms of the PI8 measurements are provided in Fig. 18 and 19, respectively. In Fig. 18, left, it is shown that the frequency of the bow shock oscillation slightly varies with thrust coefficient for the single plume case.

DOI: 10.13009/EUCASS2022-4435

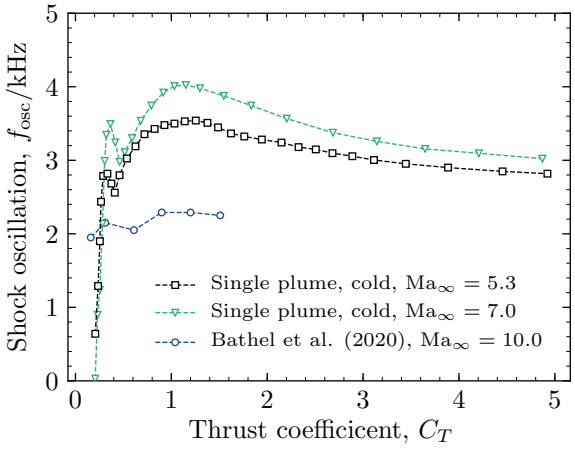

Figure 20: Comparison of shock oscillation frequencies f_{osc} over thrust coefficient C_T for hypersonic retro-propulsion with a single plume at $Ma_\infty = 5.3$ (V038) and $Ma_\infty = 7.0$ (V001) with data extracted from Bathel et al. (2020) [14] at $Ma_\infty = 10.0$

However, the intensity is not drastically influenced for $1.5 < C_T < 6.5$. The frequency steeply rises to its peak at $C_T \approx 1.2$ with a local minimum in between at $C_T \approx 0.45$. For $C_T > 1.2$, the frequency approaches a constant level at which the oscillation was measured under reference conditions. Next to the bow shock oscillation frequency and corresponding harmonics, some smaller peaks at higher frequencies were found, which are independent of the thrust coefficient and can also be detected under no plume conditions. In Fig. 19, the dependency of the spectrum along an angle of attack transient $\alpha = [0, -5, 10, 0]^\circ$ is shown, which is provided for reference at the top of the Figure. Following this evaluation, the pressure fluctuations on the main cylinder are highly depending on the angle of attack, meaning that the power spectral density rises by about one order of magnitude between zero angle of attack (see Fig. 16, 18) and -5° or $+10^\circ$ for the single plume case. For the multi-plume cases, since no peaks appear in the cylinder wall pressure spectra, only the global noise level seems to be slightly modulated by changes in C_T or α. It increases constantly with thrust coefficient and in the direction of increasing angle of attack (see Fig. 18, 19, right).

A similar investigation of the dynamics of a retro-propulsive jet, based on spectral analysis of high-speed Schlieren recordings was performed for different thrust coefficients in a Mach 10 freestream in [14]. In Fig. 20, the course of the bow shock oscillation frequency f_{osc} versus C_T is compared with extracted data points from Fig. 18 at Mach 5.3 and data from a similar test case at Mach 7 (not presented in this paper). The qualitative course of the data from [14] is comparable with the data presented here, however, the maximum frequency is lower and the local minimum is shifted to a higher $C_T \approx 0.6$. The Figure suggests that the freestream Mach number influences the dynamics, although the trend from Mach 5.3 to 10 is not continuous in this case. It is to be noted that many other parameters could also influence this phenomenon and that it is not intended to claim the Mach number to be the governing parameter. A systematic study would have to be performed in order to find the proper scaling parameter.

In this regard, a useful hint could be found in [7], where it is reported of a periodic vortex shedding from the Mach disc through the contact surface, leading to periodic flow field disturbances. This process was also detected by the authors of [7] in experimental data of [9] and in a video [16], belonging to data from a *direct numerical simulation* (DNS) in [17].

4. Conclusion and Outlook

The re-entry burn of the vertical take-off vertical landing reusable launch vehicle concept, RETPRO, was investigated experimentally in the Hypersonic Wind Tunnel Cologne (H2K) of DLR. Results from Schlieren imaging as well as force and unsteady wall pressure measurements are provided as input for CFD validation studies within the project. Additionally, a characterization of the retro-propulsion flow field, its topological modes and dynamic flow features was performed using modal analysis of high-speed Schlieren recordings. The investigations include a variation of the number of active engines and the plume temperature for different thrust coefficients and angles of attack.

It was found that the plume characteristics depend largely on the number of active engines, while a highly unsteady flow field is encountered for three active engines in contrast to a quasi-steady flow with overlaying periodic oscillation of the shock structure in the single engine case. The single plume flow topology is similar to the blunt mode referred to in literature, while the three engine case shows random flipping between a short and a long penetration

DOI: 10.13009/EUCASS2022-4435

mode. The temporal characteristics of the mode flipping is modified by increasing the plume temperature such that the short penetration mode becomes more dominant and the flipping rate is reduced. The periodic shock oscillation is found to be depending on the thrust coefficient, the freestream Mach number and the plume temperature. For thrust coefficients $1.2 < C_T < 5$, the corresponding oscillation frequency ranges from 2.8 kHz to 3.6 kHz at $\mathrm{Ma}_\infty = 5.3$ and 3.0 kHz to 4.2 kHz at $\mathrm{Ma}_\infty = 7$. It is shifted to higher frequencies under hot plume conditions. Oscillation frequencies are compared with literature, showing similar trends at a different frequency level. As a first means of explaining such variation and in order to find scaling laws, it is suggested to perform systematic studies under consideration of the underlying physics of a periodic vortex shedding mechanism in the vicinity of the terminal shock and interface, reported in literature.

The current work is performed in the context of an investigation of a complete descent trajectory of the RETPRO configuration, including the hypersonic re-entry burn at Mach 7.0 and 5.3 in the H2K, an aerodynamic descent at Mach 4.2, 3.6 and 2.0 in the *Trisonic Wind Tunnel* (TMK), as well as the subsonic landing burn between Mach 0.9 and 0.4 in the *Vertical Wind Tunnel* (VMK) using both, pressurized air and hydrogen–oxygen–combustion for simulation of the propulsive jet. The current paper represents the first publication in the experimental context while further documentation on the TMK and VMK tests is forseen. For more information on the hypersonic and supersonic tests, it is referred to another work focusing on CFD rebuilding of specific test cases for code validation and further insight.

Acknowledgments

The RETPRO project, under which the disclosed research and authorship was conducted, is carried out under a programme of and funded by the European Space Agency – through the Future Launchers Preparatory Programme (FLPP).

References

[1] Préaud, J.-P., Dussy, S., Breteau, J., and Bru, J. “Preparing the Future of European Space Transportation: Reusable Technologies and Demonstrators”. In: *8th European Conference for Aeronautics and Space Sciences (EUCASS)*. Madrid, Spain, July 2019.

[2] Kirchheck, D., Marwege, A., Klevanski, J., Riehmer, J., Gülhan, A., Karl, S., and Gloth, O. “Validation of Wind Tunnel Test and CFD Techniques for Retro-propulsion (RETPRO): Overview on a Project within the Future Launchers Preparatory Programme FLPP”. In: *International Conference on Flight Vehicles, Aerothermodynamics and Re-Entry Missions and Engineering (FAR)*. Monopoli, Italy, Sept. 2019.

[3] Colwall, S. *Shield of fire*. Photograph of SpaceX Falcon 9 flight no. 99 during its re-entry burn to Vandenberg Space Force Base. Online, 21 November 2020. URL: https://flickr.com/photos/135081788@N03/50629374248.

[4] SpaceX. *SpaceX Falcon 9 CRS-11 Launch and Landing*. Online, 4 June 2017. Re-entry burn at 11 min, 28 s, URL: https://youtu.be/ST76lGJ0UWA?t=688, landing burn at 12 min, 28 s, URL: https://youtu.be/ST76lGJ0UWA?t=748.

[5] Bykerk, T., Kirchheck, D., and Karl, S. “Reconstruction of Wind Tunnel Tests using CFD for a Reusable First Stage during Rocket Retro-Propulsion”. In: *9th European Conference for Aeronautics and Space Scicences (EUCASS)*. Lille, France, June 2022.

[6] Marwege, A., Gülhan, A., Klevanski, J., Riehmer, J., Karl, S., Kirchheck, D., Bonetti, D., Vos, J., Jevons, M., Krammer, A., and Carvalho, J. “Retro Proppulsion Assisted Landing Technologies (RETALT): Current Status and Outlook of the EU Funded Project on Reusable Launch Vehicles”. In: *70th International Astronautical Congress (IAC)*. Washington, D.C., Oct. 2019.

[7] Marwege, A., Kirchheck, D., Klevanski, J., and Gülhan, A. “Hypersonic Retro Propulsion for Reusable Launch Vehicles Tested in the H2K Wind Tunnel”. In: *CEAS Space Journal* (2022).

[8] Marwege, A., Hantz, C., Vos, J., Laureti, M., Karl, S., Kirchheck, D., Klevanski, J., and Gülhan, A. “Aerodynamic Phenomena of Retro Propulsion Descent and Landing Configurations”. In: *International Conference on Flight Vehicles, Aerothermodynamics and Re-Entry Missions and Engineering (FAR)*. Heilbronn, Germany, June 2022.

[9] Gutsche, K., Marwege, A., and Gülhan, A. “Similarity and Key Parameters of Retropropulsion Assisted Deceleration in Hypersonic Wind Tunnels”. In: *Journal of Spacecraft and Rockets* 58.4 (July 2021), pp. 984–996.

DOI: 10.13009/EUCASS2022-4435

[10] German Aerospace Center (DLR), Supersonic and Hypersonic Technologies Department. *Retro-propulsion assisted descent of a launcher in the H2K at Mach 7*. Online, February 2021. URL: https://www.dlr.de/as/portaldata/5/resources/videos/Dlr-Esa-Retpro-Retro-Propulsion-Assisted-Descent-At-Mach-7.0__Openclose__Lq-1.m4v.

[11] Finley, P. J. "The flow of a jet from a body opposing a supersonic free stream". In: *Journal of Fluid Mechanics* 26.2 (1966), pp. 337–368.

[12] Korzun, A. M., Cruz, J. R., and Braun, R. D. "A Survey of Supersonic Retropropulsion Technology for Mars Entry, Descent, and Landing". In: *IEEE Aerospace Conference*. Big Sky, Montana, Mar. 2008, pp. 1–15.

[13] Venkatachari, B. S., Cheng, G., Chang, C.-L., Zichettello, B., and Bilyeu, D. L. "Long Penetration Mode Counterflowing Jets for Supersonic Slender Configurations – A Numerical Study". In: *AIAA Fluid Dynamics Conference and Exhibit*. San Diego, California, June 2013.

[14] Bathel, B. F., Litzner, C. R., Jones, S. B., Berry, S. A., Smith, N. T., and Garbeff, II, T. J. "High-Speed Schlieren Analysis of Retropropulsion Jet in Mach 10 Flow". In: *Journal of Spacecraft and Rockets* 57.1 (Jan. 2020), pp. 33–48.

[15] Jarvinen, P. O. and Adams, R. H. *The Aerodynamic Characteristics of Large Angled Cones with Retrorockets*. Tech. rep. MC 70-3001-R2. Washington, D.C.: National Aeronautics and Space Administration (NASA), Feb. 1970.

[16] Montgomery, K. A. *Video of direct numerical simulation, presented in Montgomery et al. (2022)*. Online, January 2022. URL: https://www.linkedin.com/posts/kieran-montgomery-38abb2210_aiaascitech-activity-6890063017288048640-AoAT.

[17] Montgomery, K. A., Bruce, P. J., and Navarro-Martinez, S. "Dynamics of varying thrust coefficients for supersonic retropropulsion during Mars EDL". In: *AIAA SCITECH 2022 Forum*. San Diego, California, Jan. 2022.